Journal of Quantitative Spectroscopy & Radiative Transfer 247 (2020) 106954

Contents lists available at ScienceDirect

Journal of Quantitative Spectroscopy & Radiative Transfer

journal homepage: www.elsevier.com/locate/jqsrt

# A low-light radiative transfer model for satellite observations of moonlight and earth surface light at night

Min Min [a,b], Jianyu Zheng [c,*], Peng Zhang [d], Xiuqing Hu [d], Lin Chen [d], Xi Li [e], Yu Huang [f], Lin Zhu [d]

[a] School of Atmospheric Sciences and Guangdong Province Key Laboratory for Climate Change and Natural Disaster Studies, Sun Yat-Sen University and Southern Marine Science and Engineering Guangdong Laboratory (Zhuhai), Zhuhai 519082, China
[b] Key Laboratory of Middle Atmosphere and Global Environment Observation, Institute of Atmospheric Physics (LAGEO/IAP), Chinese Academy of Sciences, Beijing 100029, China
[c] Department of Physics, University of Maryland at Baltimore County (UMBC), Baltimore, MD 21250, United States
[d] Key Laboratory of Radiometric Calibration and Validation for Environmental Satellites (LRCVES/CMA), National Satellite Meteorological Center, China Meteorological Administration (NSMC/CMA), Beijing 100081, China
[e] State Key Laboratory of Information Engineering in Surveying, Mapping and Remote Sensing (LIESMARS), Wuhan University, Wuhan 430072, China
[f] Changchun Institute of Optics, Fine Mechanics and Physics, Chinese Academy of Sciences, Changchun, Jilin 130033, China

ARTICLE INFO

*Article history:*
Received 1 December 2019
Revised 9 March 2020
Accepted 9 March 2020
Available online 10 March 2020

*Keywords:*
Day/night band
Radiative transfer model
Lunar irradiance
Surface light

ABSTRACT

Lunar sun-reflected light can be effectively measured through a low-light band or a day/night band (DNB) implemented on space-based optical sensors. Based on moonlight, nocturnal observations for artificial light sources at night can be achieved. However, to date, an open-sourced and mature Low-Light Radiative Transfer Model (LLRTM) for the further understanding of the radiative transfer problem at night is still unavailable. Therefore, this study develops a new LLRTM at night with the correction of the lunar and active surface light sources. First, the radiative transfer equations with an active surface light source are derived for the calculation based on the lunar spectral irradiance (LSI) model. The simulation from this new LLRTM shows a minimal bias when compared with the discrete ordinates radiative transfer (DISORT) model. The simulated results of radiance and reflectance at the top of the atmosphere (TOA) also show that the surface light source has a remarkable impact on the radiative transfer process. In contrast, the change in the lunar phase angle has minimal influence. Also, comparing with space-based DNB radiance observations, LLRTM shows the potential to simulate space-based low-light imager observations under an effective surface light source condition during the night.

## 1. Introduction

In a clear night sky, natural light remains strong because of a unique light source—the moon, which can reflect solar light to the Earth's surface directly. The moon's sun-reflected light can be effectively measured by using a low-light band or day/night band (DNB), which is implemented on some custom-designed and advanced satellite optical sensors, such as the Operational Linescan System (OLS) [1–3]. Compared with relatively stable solar spectral irradiances, the extremely low magnitudes of periodical variation of lunar spectral irradiance (from $10^{-9}$ to $10^{-7}$ $\mathrm{W{\cdot}m^{-2}{\cdot}sr^{-1}}$) is correlated with lunar phase angle changes, Sun-Earth-Moon geometries and, in particular, the lunar phase-dependent moon surface materials (or albedo) [4,5]. Nevertheless, the nocturnal observation for artificial light sources at night using data collected by the U.S. Air Force Defense Meteorological Satellite Program (DMSP) Operational Linescan System has been investigated since 1976 [1,6,7]. For the low-light band, a Photo Multiplier Tube (PMT) was used to record the signal with a broad spectral response (440–940 nm). The visible band signal (500–650 nm) illuminated from the reflection of moonlight by clouds has the highest PMT sensitivity. In addition, this low-light band also covers the range for primary emissions from the most widely used surface lamps: mercury vapor (545 nm and 575 nm), high-pressure sodium vapor (from 540 nm to 630 nm), low-pressure sodium vapor (589 nm), etc. [2,6,8].

The successor of the DMSP/OLS, an advanced Day/Night Band (DNB) on the Visible Infrared Imaging Radiometer Suite (VIIRS) onboard the NOAA (National Oceanic and Atmospheric Administration) Suomi National Polar-orbiting Partnership (SNPP) satellite was successfully launched on 28 October 2011 [9,10]. The first dedicated nighttime light remote sensing satellite in the world,

---

[*] Corresponding author.
*E-mail address:* jzheng3@umbc.edu (J. Zheng).

https://doi.org/10.1016/j.jqsrt.2020.106954

the LuoJia1-01 satellite, led by Wuhan University, was successfully launched on 2 June 2018 [11]. In addition, a new DNB will be onboard FengYun-3 (FY-3) Early-Morning-Orbit satellite's Medium Resolution Spectral Imager (MERSI), which is scheduled to launch in 2020 [12–15]. The space-based DNB observations not only allow users to examine social and economic activities at urban scales or monitor hurricanes [2,16–19], but can also provide high-quality sub-pixel cloud test information for passive microwave and infrared hyperspectral sensors, which act as a critical data source for data assimilation modules in numerical weather prediction modeling [9,20,21].

According to previous research, compared with infrared band observations, the DNB observations can capture more details of the Earth's surface through relatively weak lunar reflected light at night [22]. It attempts to retrieve nighttime optical depth and microphysical features of aerosols and clouds by using the VIIRS/DNB measurements. This study shows the dependency of the retrieval on different regions, for example, those with and without artificial surface lights [23,24]. However, the increasing number of artificial lights at the surface, primarily in urban areas resulting in increasing radiance, has a notable impact on cloud and aerosol retrievals from space-based DNB observations [16]. Nevertheless, the basic radiative transfer model at night does not perform well in processing data containing surface light sources in the visible band, such as the retrieval of cloud nighttime optical depth [25,26]. The Low-Light Radiative Transfer Model (LLRTM) at night is one of the essential prerequisites and tools for promoting practical quantitative applications of space-based DNB data. However, the current version of LLRTM does not take into account the surface anthropological light source, and it is still a test version. [25].

Therefore, the primary goal of this investigation is to develop a new LLRTM with corrections for lunar and active surface light sources. The next sections will introduce the derivation of the low-light radiative transfer equations with lunar and active surface light sources. The validation results for the new LLRTM are shown in the Appendix section. The following sections will demonstrate the comparison of simulated radiance and reflectance at the TOA between LLRTM with and without effective surface light sources. The contrast between the developed LLRTM simulations and VIIRS/DNB observations will also be discussed. Finally, significant findings will be summarized.

## 2. Theory basis

### 2.1. Fundamentals of lunar radiative transfer

First, we reviewed the fundamentals of traditional atmospheric radiative transfer under a solar incident condition [27]. In essence, the physical processes of radiative transfer between a conventional solar reflective RTM and a new RTM with a lunar irradiance source at night are nearly the same, except for solar and lunar sources, which have different intensities of irradiance and distances with Earth [25]. Besides, a plane-parallel solar irradiance at the top of the atmosphere is assumed by ignoring the field angle (0.0025°) between the radius of Earth with the Sun/Earth perihelion distance, as shown in Fig. 1a. In this study, the field angle (1.02°) between the radius of Earth with the Moon/Earth perigee distance probably lead to a slight bias of lunar irradiance in the low-latitude regions (as shown in Fig. 1b) if we assume a plane-parallel atmosphere. However, this slight bias can be corrected by adjusting the lunar zenith angle in terms of the variation of latitude [5,28]. The application of lunar radiance, in most cases, outweighs the detraction due to the plane-parallel assumption in the radiative transfer model [5].

Nevertheless, the primary objective of this study is to explore a new radiative transfer method for calculating upward surface light flux. Thus, we do not consider this slight bias from the lunar irradiance model, which will be systematically discussed in the future. Moreover, although the polarized information of lunar light is not taken into account in the first simulation results, it will be considered in the further applications in specific regions, especially the highly light-polluted areas [29].

Fig. 2 shows a schematic diagram of radiative transfer of diffuse lunar radiance with artificial light sources at the surface at night at the bottom in plane-parallel layers. Note that, this study primarily describes the monochromatic lunar radiative transfer process (wavelength<3.5 μm). Thus, the wavelength notation or index, $\lambda$, and thermal emission term, $B[T(z)]$, are neglected. In this thermal emission term, $T(z)$ represents the temperature at the altitude of $z$, which can be calculated using Planck's law.

Based on Fig. 2 and definitions of solar reflective radiative transfer [27], we re-write the diffuse lunar radiative transfer equation as follows:

$$\frac{\Delta I(z;\mu,\phi)}{\Delta z/\mu} = -\beta_e I(z;\mu,\phi) + \beta_s F_0 e^{-\tau/\mu_0}\cdot P(\mu,\phi;-\mu_0,\phi_0)/4\pi + \beta_s\int_0^{2\pi}\int_{-1}^{1} I\big(z;\mu',\phi'\big)\cdot P\big(\mu,\phi;\mu',\phi'\big)/4\pi\, d\mu' d\phi', \tag{1}$$

In Eq. (1), $\Delta I$ and $\Delta z$ on the left-hand side respectively represent the differential flux beam and geometry thickness in Fig. 2. The three terms on the right-hand side of Eq. (1) and Fig. 2 respectively represent (1) the attenuation by extinction of lunar flux, $I_0$, (2) the single scattering of the direct lunar flux, $I_{0,s}$ (subscript "$s$" means single scattering), and (3) the multiple scattering of lunar flux, $I_{0,m}$(subscript "$m$" means multiple scattering). $\beta_e$ and $\beta_s$, respectively, signify extinction and scattering coefficients. $F_0$ represents lunar incident irradiance, which replaces the original solar constant irradiance in this formula. The symbols of $\mu$,$\phi$,$\mu_0$,$\phi_0$ represent the lunar cosine of zenith angle, the lunar azimuth angle, the cosine of view zenith angle, and the view azimuth angle, respectively. As an important parameter in RTM, $\phi = \phi_0 - \phi$ is the relative azimuth angle, which ranges from 0° to 180°. $P$ is the phase function, representing the angular distribution of the scattered energy as a function of the scattering angle, $\Theta$, for scattering medium (i.e., aerosols or cloud particles), whose integral is equal to 1.

Further, we define single scattering albedo, $\omega$, and optical depth, $\tau$, in the forms:

$$\omega = \beta_s/\beta_e, \tag{2}$$

$$\tau = \int_z^{\infty}\beta_e(z')dz', \tag{3}$$

Based on the term of $\tau$, the Eq. (1) can be rewritten as follows:

$$\mu\frac{dI(\tau;\mu,\phi)}{d\tau} = I(\tau;\mu,\phi) - \frac{\omega}{4\pi}F_0 P(\mu,\phi;-\mu_0,\phi_0)e^{-\tau/\mu_0} - \frac{\omega}{4\pi}\int_0^{2\pi}\int_{-1}^{1} I(\tau;\mu',\phi')P(\mu,\phi;\mu',\phi')d\mu' d\phi', \tag{4}$$

where the last two terms on the right-hand side are known as the source function, $J$, which is associated with single and multiple scattering processes. Therefore, Eq. (4) can be simplified as follows:

$$-\mu\frac{dI}{d\tau} = -I + J, \tag{5}$$

This differential form equation briefly describes the variation of radiance, $I$, with a thin extinction layer of $d\tau$.

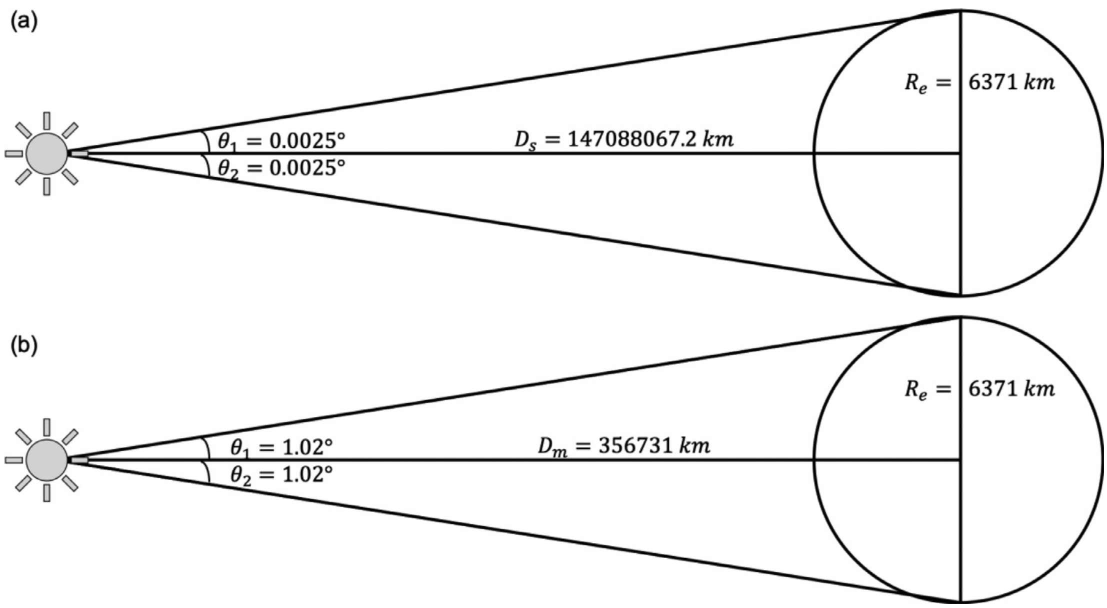

**Fig. 1.** Geometric diagram of the calculation of the angle of solar radiation beams (a) and lunar radiation beams (b) with the radius of Earth. $D_s$, $D_m$ and $R_e$ represent the Sun/Earth perihelion distance, the Moon/Earth perigee distance and the averaged radius of Earth, respectively.

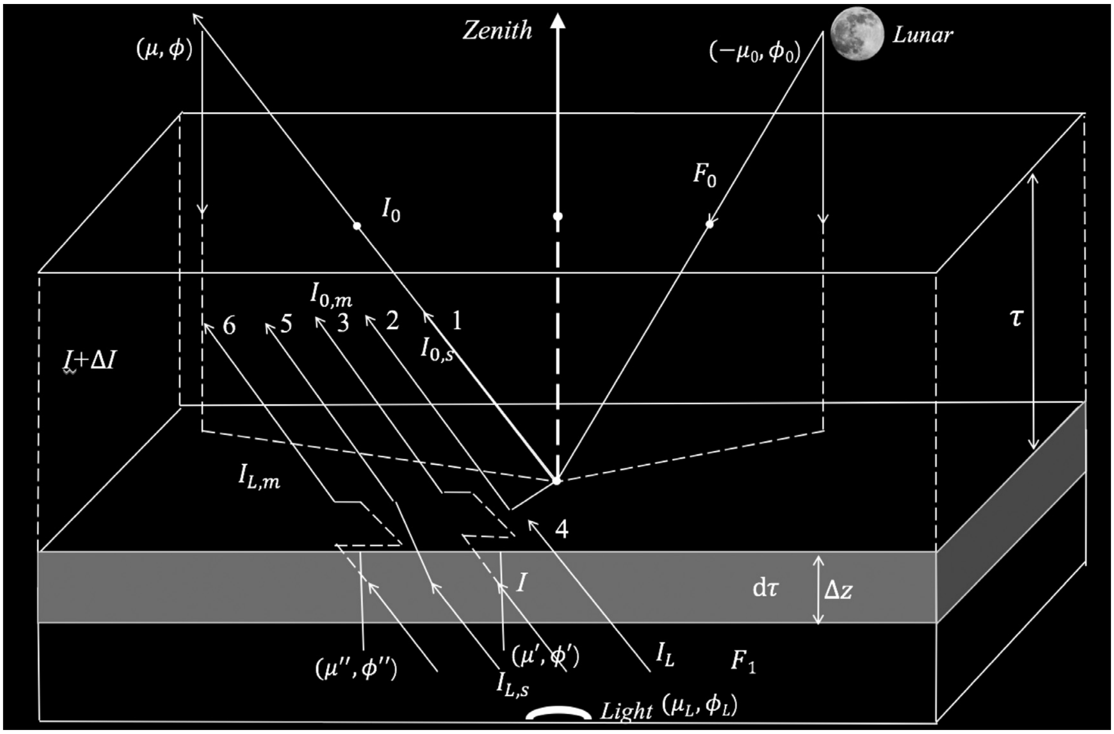

**Fig. 2.** Schematic diagram of radiative transfer of diffuse lunar intensity with a surface light source at night from below in plane-parallel layers (modified according to the original figure 3.16 in [27]): (1) attenuation by extinction of lunar flux; (2) single scattering of the unscattered lunar flux; (3) multiple scattering of lunar flux; (4) attenuation by extinction of the upward surface light flux; (5) single scattering of the upward surface light flux; and (6) multiple scattering of the upward surface light flux. These parameters are defined concerning a differential thickness $\Delta z$. The notations are defined in Section 2.

### 2.2. Lunar spectral irradiance model

As mentioned above, theoretically, the atmospheric radiative transfer process at night replaces the solar source with a new lunar irradiance source ($F_0$) in Eq. (4). Therefore, before introducing a surface light incident term into the radiative transfer, we use a dynamic lunar spectral irradiance (LSI) model developed by Miller and Turner in 2009 [as the citation] to replace the constant solar irradiance model [5] in Eq. (4).

The LSI model, official support for the current NOAA JPSS/VIIRS-DNB data application [7,22], can accurately and rapidly simulate lunar spectral irradiances ($F_0$) at the TOA ranging from 0.202 µm to 2.80 µm with 1 nm resolution. The lunar irradiance is a function of the lunar phase angle periodical changes, and the Sun-Moon-Earth geometries [5]. The simulated incident irradiance at the TOA can be written as follows:

$$F_0 = \alpha E_0 \left(\frac{\overline{R_{se}}}{R_{sm}}\right)\left(\frac{r_m}{R_{me} - r_e}\right) f(\theta), \tag{6}$$

where $\alpha$ represents the mean lunar visual albedo ($0.105<\alpha<0.125$), and the symbol of $E_0$ is the constant solar irradiance. The product of the first two terms explicitly illustrates that the moon directly reflects the incident sunlight at night. The five terms $\overline{R_{se}}$, $R_{sm}$, $R_{me}$, $r_m$, and $r_e$ are geometry factors, which respectively signify the mean Sun-Earth distance, the Sun-Moon distance, the Moon-Earth distance, the radius of the Moon and the radius of the Earth. As another important impact factor on lunar brightness, the last term $f(\theta)$ is the phase function of the lunar phase angle $\theta$ [5].

### 2.3. Radiative transfer calculation with an active surface light source

In this investigation, the primary objective is to develop a low-light radiative transfer model at night based on the plane parallel assumption, which can conduct precise radiative transfer calculations with lunar and surface light incident sources. Although the three-dimensional (3D) effect from surface light source probably impacts on simulation process, we simplify the 3D RT problem to a 1D RTM in this investigation with an effective surface light source (see Eq. (11)). However, the validation of the 1D-assumed RTM with 3D RTM models is important but remains to be done in the next step, which will not be included in this study. According to the Eq. (5), the differential radiance $dI$ with a new light flux beam from the surface can be rewritten as:

$$-\mu\frac{dI+dI_L}{d\tau}=-I+J-I_L+J_L, \tag{7}$$

where the last two terms on the right-hand side $I_L$ and $J_L$ (subscript "$L$" means surface light) respectively represent the direct extinction and source function for surface light flux beam.

Like the reflected lunar flux beam in Eq. (4), the term $J_L$ also contains both single and multiple scattering contributions for the surface light flux beam. Fig. 2 also shows attenuation by the extinction term (label 4), the single-scattering term (label 5), and the multiple scattering term of the upward surface light flux (label 6). Fig. 2 demonstrates that the microscopic radiative transfer process of emitted surface light, in reality, especially urban light source, is very complicated. That radiative transfer process includes the direct flux beam and the single/multiple scattering and absorption at the surface or on buildings. Some preview studies [30,31] simulate urban albedo or radiative transfer processes within three-dimensional structures based on a Monte Carlo model. These numerical simulations are time-consuming and difficult to embed in an atmospheric RTM. Therefore, to develop a new source function in Eq. (7), a simplified scheme should be proposed here to describe the contribution of surface light sources.

Next, this study will discuss how to develop an original source function to incorporate surface light sources into the radiative transfer calculation in RTM. First, the term $-\mu\cdot(dI/d\tau)$ on the left-hand side of Eq. (7) can be separated and described as:

$$-\mu\frac{dI}{d\tau}=-\mu\frac{d(I_0+I_L)}{d\tau}=-\mu\left(\frac{dI_0}{d\tau}+\frac{dI_L}{d\tau}\right)=-\mu\frac{dI_0}{d\tau}-\mu\frac{dI_L}{d\tau}, \tag{8}$$

where $I_0$ and $I_L$ respectively represent the contributions from lunar and surface light flux beams. According to this equation, Eq. (4), and Fig. 2, we propose a new and simplified effective surface light irradiance term, $F_1$, to represent all the contributions from the surface light flux beams, which can calculate the direct plane parallel flux from the surface layer. Thus, the current radiative transfer equation with both lunar and surface light sources can be rewritten as follows:

$$\begin{aligned}\mu\frac{dI_0(\tau;\mu,\phi)}{d\tau}+\mu\frac{dI_L(\tau_L;\mu,\phi)}{d\tau}&=I_0(\tau;\mu,\phi)\\&-\frac{\omega}{4\pi}F_0P(\mu,\phi;-\mu_0,\phi_0)e^{-\tau/\mu_0}\\&-\frac{\omega}{4\pi}\int_0^{2\pi}\int_{-1}^{1}I_0(\tau;\mu\prime,\phi\prime)P(\mu,\phi;\mu\prime,\phi\prime)d\mu\prime d\phi\prime\\&+I_L(\tau_L;\mu,\phi)-\frac{\omega}{4\pi}F_1P(\mu,\phi;\mu_L,\phi_L)e^{-\tau_L/\mu_L}\\&-\frac{\omega}{4\pi}\int_0^{2\pi}\int_{-1}^{1}I_L(\tau_L;\mu'',\phi'')P(\mu,\phi;\mu'',\phi'')d\mu\prime\prime d\phi\prime\prime,\end{aligned} \tag{9}$$

where the new symbols of $\mu_L$ and $\phi_L$ are the cosine of zenith and azimuth angles of the effective surface light source, respectively. Note that, due to the different radiative transfer processes of moonlight and surface light, we define a new optical depth of $\tau_L$ for the upward flux of surface light source in this equation. However, the single scattering albedo of $\omega$ for the same optical extinction layer is a constant. Theoretically, from Fig. 2, we assume that the observed pixel from a space-based DNB sensor has the same horizontal position as the surface light source. Thereby, the azimuth angle of active surface light, $\phi_L$ is always equal to 0°. We also assume that the effective surface light flux is perpendicular to the surface in a plane-parallel atmosphere, which implies the zenith angle for $\mu_L$ is also equal to 0°. Based on these assumptions, we can extract the effective surface light radiative transfer process from Eq. (9) as follows:

$$\begin{aligned}\mu\frac{dI_L(\tau_L;\mu,\phi)}{d\tau}&=I_L(\tau_L;\mu,\phi)-\frac{\omega}{4\pi}F_1P(\mu,\phi;0,0)e^{-\tau_L}\\&-\frac{\omega}{4\pi}\int_0^{2\pi}\int_{-1}^{1}I_L(\tau_L;\mu'',\phi'')P(\mu,\phi;\mu'',\phi'')d\mu\prime\prime d\phi\prime\prime,\end{aligned} \tag{10}$$

From Eq. (10), we find the surface light source radiative transfer process can be seen as an independent radiative transfer equation. Hence, how to calculate the effective surface light irradiance, $F_1$ becomes a key challenge of the surface light radiative transfer simulation. Unfortunately, there are no relevant studies about real surface light irradiance observations from any literature. However, some researchers [3,8] who work on nighttime satellites' remote sensing applications have already measured and summarized primary types of worldwide used outdoor artificial lighting, including incandescent, mercury vapor lamps, low-pressure/high-pressure sodium vapor lamps, metal halide lamps, and light-emitting diode (LED). These distinctive spectral signatures can be found from radiance measurements of the various types of outdoor light sources [8].

We find some spectral radiance measurements of various types of outdoor light sources using the Analytical Spectral Device (ASD) spectroradiometer (https://discover.asdi.com/bid/48919/Spectral-Signatures-of-Nighttime-Lights). In this study, we choose three typical outdoor lights to make an effective surface light source as a test for LLRTM, including high-pressure sodium vapor, incandescent, and LED. Fig. 3 shows the vertical upward spectral radiances and signatures of these three types of outdoor light measured by the ASD spectroradiometer (all the values are extracted from the ASD measurement result pictures). From this figure, we find significant differences in radiance magnitude and spectral signature between the three different outdoor lights. For instance, there are many peaks at the wavelengths < 1500 nm for the spectral radiance of high-pressure sodium vapor light in comparison to the smooth spectral signatures of incandescent and LED. Nevertheless, the total radiance measured from the space-based low-light band is a mix of different surface outdoor light sources and their quantities. Therefore, in light of the definition of irradiance, we define a simple weighting equation here to calculate the final irradiance of the effective surface light source [32].

$$F_1=\sum_{i=1}^{n}w_i\pi L_i, \tag{11}$$

where $L_i$ and $w_i$ respectively represent the upward radiance of $n$th outdoor surface light and the corresponding weight value. More-

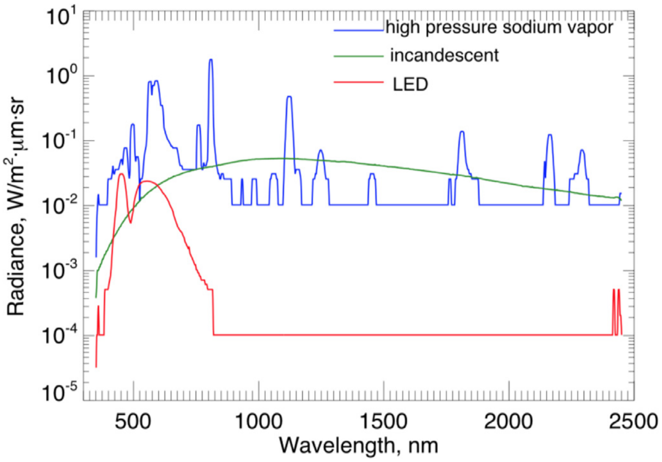

**Fig. 3.** Vertical upward spectral radiances and signatures of three types of outdoor light (blue: high-pressure sodium vapor, green: incandescent, and red: LED) measured by ASD spectroradiometer.

over, remarkably like an amplification factor, this weight value can be larger than 1.0, which means the increase of surface light flux intensity. However, only three types of surface light radiance will be used here to calculate the final irradiance of the effective surface light source. Note that the constant term of $\pi$ (before $L_i$) in Eq. (11) is to convert radiance (W/m$^2$·µm·sr) of $L_i$ in a semispherical space to irradiance (W/m$^2$·µm) under the plane-parallel and isotropic property assumption.

After that, we develop a new hyper-spectral RTM (or LLRTM) under the plane-parallel condition with both the lunar and active surface light sources mentioned above to simulate the radiance and reflectance observed by the low-light band or DNB from space. The Appendix section elucidates and validates the LLRTM, which uses a classical adding-doubling (AD) method [27,33] to solve the RT equation for two different incident radiation sources.

## 3. Simulation results

### 3.1. Radiances and reflectance at the TOA

Like previous study [25], we simulate the spectral radiance and reflectance (see Eq. (29)) of clear sky at the TOA from 0.4 to 2.0 µm with the lunar irradiance source using LLRTM under four lunar phase angles of $\theta = 0°$, 45°, 90°, and 135° in Fig. 4. Lunar zenith angle, view zenith angle, and relative azimuth angle respectively equal to 20°, 10°, and 0° This model considers seven

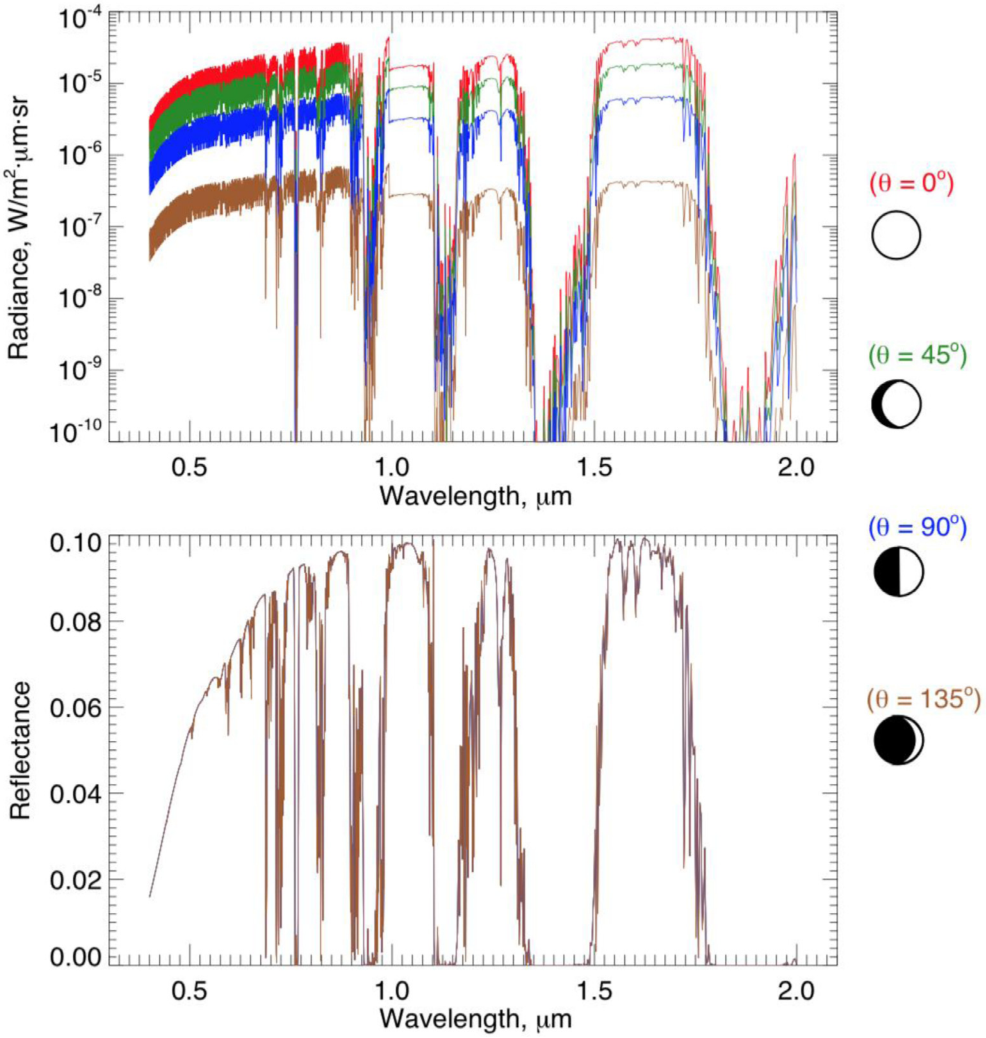

**Fig. 4.** Simulated spectral radiances (top panel) and reflectance (bottom panel) at the TOA from 0.4 to 2.0 µm with the lunar irradiance source using LLRTM under four different lunar phase angles of $\theta$ =0° (in red), 45° (in green), 90° (in blue), and 135° (in brown). Lunar zenith angle (LZA), view zenith angle (VZA), and relative azimuth angle respectively equal to 20°, 10°, and 0°.

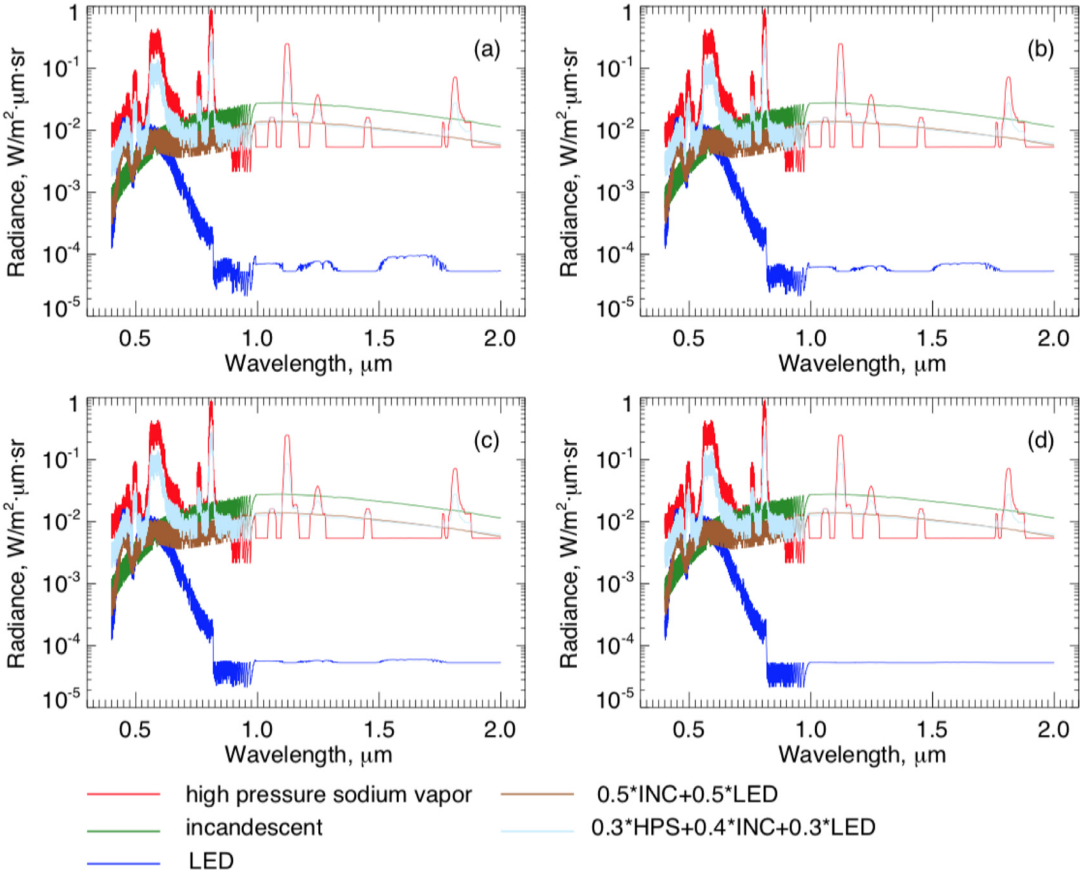

**Fig. 5.** Simulated spectral radiances at the TOA from 0.4 to 2.0 μm with both lunar irradiance and effective surface light sources using LLRTM under four different lunar phase angles of $\theta$ =0° (a), 45° (b), 90° (c), and 135° (d). Observation geometry conditions are the same as those of Fig. 4. Red, green, blue, brown, and light blue solid lines respectively represent the cases with high-pressure sodium vapor (HPS), incandescent (INC), LED, and two mixed light sources.

major atmospheric absorptive gases ($H_2O$, $CO_2$, $O_3$, $O_2$, $CH_4$, CO, and $N_2O$) based on a rigorous line-by-line (LBL) radiative transfer model (LBLRTM), and a parameterization calculation of Rayleigh scattering optical depth [34,35]. The mid-latitude summer atmospheric profile data is used here to calculate the gas absorption optical depths for each atmospheric layer and a Lambert surface with an albedo of 0.05.

From the sub-figure in the top panel of Fig. 4, we find the simulated radiances at lunar phase angle $\theta = 0°$ are approximately two orders of magnitude higher than those at lunar phase angle $\theta = 135°$ because of the different intensities at different lunar phase angles, which have been demonstrated in previous studies on lunar irradiance model [5,25]. In contrast, it is not surprising that the simulated normalized reflectance at the TOA in the bottom panel of Fig. 4 shows little difference between different lunar phase angles.

In addition to the simulated clear-sky case without the surface light source mentioned above, Fig. 5 shows the simulated spectral radiances at the TOA from 0.4 to 2.0 μm with both lunar irradiance and effective surface light sources using LLRTM under four different lunar phase angles of $\theta = 0°$, 45°, 90°, and 135°. Observation geometry conditions are the same as those of Fig. 4. The red, green, blue, brown, and light blue solid lines respectively represent the cases with high-pressure sodium vapor (HPS), incandescent (INC), LED, and two mixed light sources. According to the results in this figure, the surface light source plays a dominant role in the process of atmospheric radiative transfer. The changes in the lunar phase angle (or irradiance) cannot significantly impact the radiance measured by the space-based low-light sensor. However, we still find that the changes in the lunar phase angle can slightly impact the upward radiances at the TOA of LED (blue line) from the wavelength 800 to 2000 nm.

### 3.2. Comparisons with VIIRS/DNB observations

Despite that the real emissive irradiance from a surface light source and atmospheric aerosol scattering and absorption properties are very difficult to obtain, we still hope to compare the observations from SNPP VIIRS/DNB and the simulations to test LLRTM's performance and availability. Considering the effects of variable lunar irradiance and unknown active surface light sources [5,25], we here compare the radiance at the TOA during the night, $I_{DNB}$, but not normalized reflectance at the TOA (see Eq. 36) in the Appendix section), which can be written as follows:

$$I_{DNB} = \frac{\mu F_0 \rho_{DNB}}{\pi}, \tag{14}$$

where $\rho_{DNB}$ is the reflectance observed by VIIRS/DNB or simulated by LLRTM.

From Eq. (14), $I_{DNB}$ is still a wavelength-independent variable. However, the specific radiance $L_{DNB}$(unit = W/m$^2$·sr) provided by official VIIRS/DNB data is remarkably different from $I_{DNB}$ (unit = W/m$^2$·μm·sr), which is a convolution or integrated variable with wavelength and can be written as follow:

$$L_{DNB} = \int_{\lambda_1}^{\lambda_2} RSR(\lambda) \cdot I_{DNB}(\lambda) d\lambda, \tag{15}$$

where $RSR$ represents the relative (or normalized) spectral response (from 0 to 1.0) for DNB. It is publicly available from the National Oceanic and Atmospheric Administration (NOAA) (https:

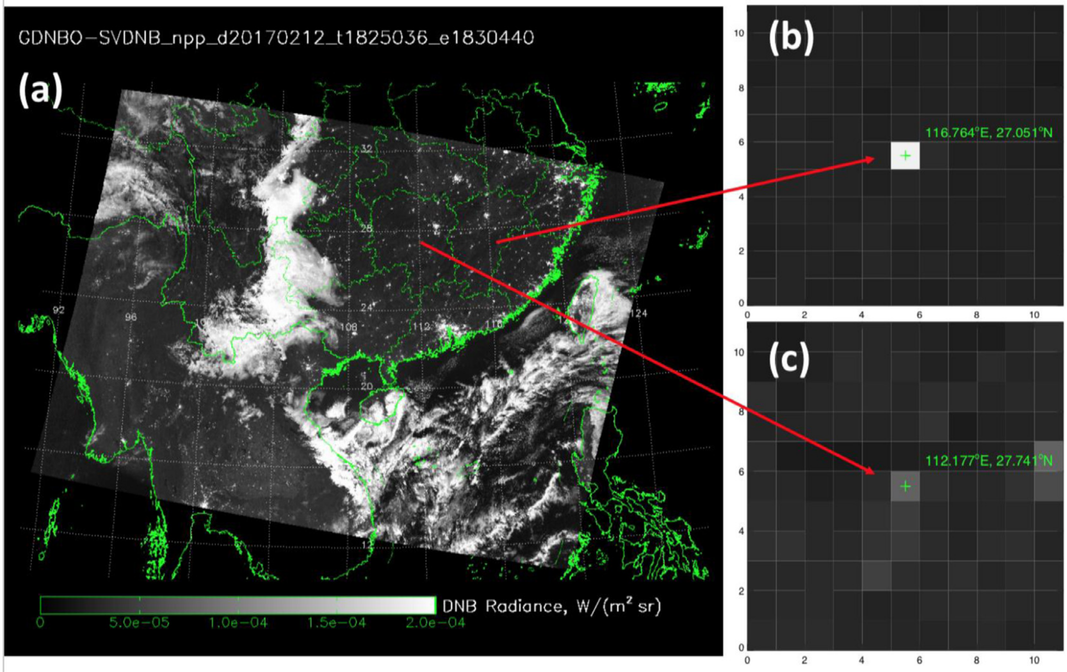

**Fig. 6.** SNPP VIIRS/DNB wavelength-integrated radiance image (a) and two interest points (b=NO. 1 at 116.764°E, 27.051°N and c=NO.2 at 112.177°E, 27.741°N) at 18:25 UTC on 12 February 2017.

**Table 1**
Coordinate (longitude/latitude), Lunar zenith angle (LZA), Lunar azimuth angle (LAA), View zenith angle (VZA), View azimuth angle (VAA), the nearest available aerosol optical depth (AOD), observed/simulated radiances for DNB, and assumed active light sources for two interest points (NO.1 and NO. 2) from Fig. 6 at 18:25 UTC on 12 February 2017. The lunar phase angle equals to 21.58°.

| Interest point | Coordinate | Geometries (LZA/LAA/VZA/VAA, °) | AOD | Observation ($W/m^2 \cdot sr$) | Simulation ($W/m^2 \cdot sr$) | Light source |
|---|---|---|---|---|---|---|
| NO. 1 | 116.764°E, 27.051°N | 22.4691/−155.79/47.0188/−76.2438 | 0.221 | 1.90705E-04 | 1.92654 E-04 | LED=0.41 |
| NO. 2 | 112.177°E, 27.741°N | 21.8544/−168.105/21.3511/−77.9384 | 0.232 | 7.79785E-05 | 7.70313E-05 | LED=0.038 |

//www.nesdis.noaa.gov), which has been used in our previous investigation [25]. $\lambda_1$ (about 400 nm) and $\lambda_2$ (about 990 nm) respectively signify the start and the end wavelengths of VIIRS/DNB. Therefore, this process should use the simulated spectral radiances to convolve DNB's *RSR* at different wavelengths to calculate integrated radiance in Eq. (15).

Fig. 6 shows the SNPP VIIRS/DNB wavelength-integrated radiance image and two points of interest within the zoomed area (NO. 1 at 116.764°E, 27.051°N and NO.2 at 112.177°E, 27.741°N) with the lunar phase angle $\theta = 21.58°$ at 18:25 UTC on 12 February 2017. From this figure, we find that both points of interest are under a clear-sky condition, and the NO.1 point is brighter than the NO. 2 point. The essential input parameters of LLRTM are listed in Table 1, including coordinates (longitude/latitude), lunar zenith angles (LZA), lunar azimuth angles (LAA), view zenith angles (VZA), view azimuth angles (VAA), the nearest available aerosol optical depths (AOD), and observation radiances for two interest points (NO.1 and NO. 2). Note that, the nearest available AOD values for two interest points are extracted from the Aqua/MODIS Collection 6.1 08 daily product. On account of that, the comparison between observation and simulation will be severely impacted by unknown active surface light-emissive irradiance. In practice, it is very hard to obtain the spatial-temporal matched local radiosonde data [36]. Thus, we use the middle latitude winter atmospheric profile to calculate gases and Rayleigh optical depth (similar to Section 3.1). As shown in the Appendix section, we also assume aerosol single scattering albedo (SSA) and asymmetry factor (AF) are respectively equal to 0.92 and 0.75 for all wavelengths. The Henyey-Greenstein scattering phase function for aerosol and a fixed surface albedo (=0.02) are input into LLRTM for simulating radiance.

According to the results of Fig. 5, we use a relatively dim LED light as the primary surface light source for a simulation. We iteratively tune the amplification factor or ratio before the surface light irradiance term (see Eq. (11)) to get closer results to observations. From Table 1, we also find the simulated integrated radiances at two interest points are respectively equal to 1.926545E-04 and 7.70313E-05 $W/m^2 \cdot sr$, which are close to the observed values of 1.90705E-04 and 7.79785E-05 $W/m^2 \cdot sr$. The corresponding amplification factors for the LED light source are 0.41 and 0.038, respectively. We think that these two different amplification factors for the LED light source illustrate the effective proportion of real surface light in one pixel with reasonable certainty. Nevertheless, the point-to-point comparisons demonstrate the new LLRTM can well simulate radiance with active surface light source observed by space-based low-light imager at night.

## 4. Conclusion

This study attempts to develop a new low-light radiative transfer model with an active surface light source and a lunar irradiance source for space-based low-light band (or DNB) measurements at night. The primary objective of this model is to promote practical quantitative applications of space-based DNB data in the future. Here, we elucidate the lunar irradiance model, the active surface light irradiance model, and how to build this low-light radiative transfer model from basic theory to code.

Validations for the LLRTM have been conducted using the DISORT model under some assumed conditions in the Appendix section. It finds a minimal bias in the simulated reflectance at the TOA between two RTMs (<0.0002 or 0.1%). After that, we test the LLRTM's performance under different lunar phases and active surface light source conditions. It exhibits variations in simulated spectral radiances due to the effects of the lunar phase and active surface light source. We also compare the radiances from VIIRS/DNB observations and LLRTM simulations, which demonstrate the possibility of simulating space-based low-light imager observations under an effective surface light source condition at night.

However, there are still some other questions that should be answered for simulating space-based DNB measurements at night in the future, which are summarized as follows:

(1) Whether aerosol's optical properties can significantly impact their bulk scattering properties and radiative transfer calculations at Day/Night Band or not? (This question is extended from our previous study on clouds at DNB [25])
(2) How to further explore the sophisticated features and measure real emitted radiances of different active surface light sources?
(3) For quantitative application, which low-light spectral band should be developed for use in a future satellite?
(4) With the assumption of the plane-parallel assumption, how different with 3D RTM model simulation will be?

## Declaration of Competing Interest

The authors have no affiliation with any organization with a direct or indirect financial interest in the subject matter discussed in the manuscript.

## CRediT authorship contribution statement

**Min Min:** Conceptualization, Data curation, Methodology, Investigation, Software, Funding acquisition, Resources, Writing - review & editing. **Jianyu Zheng:** Conceptualization, Methodology, Data curation, Investigation, Software, Writing - review & editing. **Peng Zhang:** Conceptualization, Methodology, Project administration, Supervision. **Xiuqing Hu:** Formal analysis, Resources, Supervision. **Lin Chen:** Formal analysis, Validation. **Xi Li:** Formal analysis, Resources. **Yu Huang:** Writing - review & editing. **Lin Zhu:** Writing - review & editing.

## Acknowledgments

The authors would like to acknowledge Dr. Steven Miller and Dr. Christopher D. Elvidge for making his lunar irradiance model and light intensity measurements publicly available, respectively. We thank the STEVENS Institute of Technology Laboratory (http://lllab.phy.stevens.edu/disort) and Atmospheric and Environmental Research Company (http://rtweb.aer.com/lblrtm_frame.html) for freely providing the DISORT-V2.0 and LBLRTM models. Suomi NPP VIIRS/DNB and MODIS data are freely downloaded from NOAA (https://www.avl.class.noaa.gov) and NASA (https://ladsweb.modaps.eosdis.nasa.gov) websites. This study was supported by the Ministry of Science and Technology of China under Grant 2018YFA0605502, the Open Foundation under Grant LAGEO-2019–01, the Natural Science Foundation of China under Grants 41975031, 41975020, 41775045 and 41571348, and the Pre-research Project under grant D040103. Last but not least, we would also like to thank the editor and anonymous reviewers for their thoughtful suggestions and comments.

## Appendix

Many previous atmospheric RTMs [33,37–40] commonly use the rigorous adding-doubling method to solve the RT problems under the plane-parallel condition. Numerically, the scattering phase function, $P$, and the intensity, $I$, can be expanded as a series of the Legendre polynomial with a finite number of terms, $N$, and a Fourier cosine series [27,41], which are independent (or discrete) with relative azimuth angle of $\phi$. Thus, Eqs. (7) and (8) can be rewritten as follow:

$$\mu\left(\frac{dI_0^m + dI_L^m}{d\tau}\right) = I_0^m - J_0^m + I_L^m - J_L^m,\ (m = 0, 1, 2 \ldots\ldots N), \tag{16}$$

Likewise, this equation can be written as an azimuthal-independent or discrete form:

$$\begin{aligned}\mu\frac{dI_0^m(\tau;\mu)}{d\tau} + \mu\frac{dI_L^m(\tau_L;\mu)}{d\tau} &= I_0^m(\tau;\mu)\\ &-\frac{\omega}{4\pi}F_0\sum_{l=m}^{N}\varpi_l{}^m P_l^m(\mu)P_l^m(-\mu_0)e^{-\tau/\mu_0}\\ &-(1+\delta_0^m)\frac{\omega}{4\pi}\sum_{l=m}^{N}\varpi_l{}^m P_l^m(\mu)\int_{-1}^{1} I_0^m(\tau;\mu\prime)P(\mu\prime)d\mu\prime I_L^m(\tau_L;\mu)\\ &-\frac{\omega}{4\pi}F_1\sum_{l=m}^{N}\varpi_l{}^m P_l^m(\mu)P_l^m(0)e^{-\tau_L}\\ &-(1+\delta_0^m)\frac{\omega}{4\pi}\sum_{l=m}^{N}\varpi_l{}^m P_l^m(\mu)\int_{-1}^{1} I_L^m(\tau_L;\mu\prime\prime)P(\mu\prime\prime)d\mu\prime\prime,\end{aligned} \tag{17}$$

where $P_l^m$ and $\varpi_l{}^m$ respectively denote the associated Legendre polynomials and the corresponding moments. $\delta_0^m$ is the Dirac function, which can be expressed as follow:

$$\delta_0^m = \begin{cases} 1, & m = 0 \\ 0, & m \neq 0 \end{cases}, \tag{18}$$

By Eq. (17), every azimuthally independent radiative transfer ($m = 0$) of diffuse radiation can be rewritten as follows:

$$\begin{aligned}\mu\frac{dI_0(\tau;\mu)}{d\tau} + \mu\frac{dI_L(\tau_L;\mu)}{d\tau} &= I_0(\tau;\mu) - \frac{\omega}{4\pi}F_0 P(\mu,-\mu_0)e^{-\tau/\mu_0}\\ &-\frac{\omega}{2\pi}\int_{-1}^{1} I_0(\tau;\mu\prime)P(\mu,\mu\prime)d\mu\prime I_L(\tau_L;\mu) - \frac{\omega}{4\pi}F_1 P(\mu,0)e^{-\tau_L}\\ &-\frac{\omega}{2\pi}\int_{-1}^{1} I_L\big(\tau_L;\mu''\big)P(\mu,\mu\prime\prime)d\mu\prime\prime,\end{aligned} \tag{19}$$

This equation can be easily separated into two independent terms for both lunar and the surface light sources. Therefore, the AD method will be used to solve two separate radiative transfer equations at different relative azimuth angle terms.

In the AD method, the calculations of the bidirectional reflection, $R$, and transmission, $T$, functions for an optically thin layer $\tau$ are fundamental and crucial for solving the RT equation [27]. Considering an optically thin layer (e.g., $\Delta\tau \approx 10^{-6}$), $R_0$ and $T_0$ for lunar source can be simplified to give

$$R_0(\mu,\phi;\mu_0,\phi_0) = \frac{\omega\Delta\tau}{4\mu\mu_0}P(\mu,\phi;-\mu_0,\phi_0), \tag{20}$$

$$T_0(\mu,\phi;\mu_0,\phi_0) = \frac{\omega\Delta\tau}{4\mu\mu_0}P(-\mu,\phi;-\mu_0,\phi_0), \tag{21}$$

Similarly, for the active surface light source at the bottom, the $R_L$ and $T_L$ terms are expressed as follows:

$$R_L(\mu,\phi;0,0) = \frac{\omega\Delta\tau_L}{4\mu\mu_0}P(-\mu,\phi;0,0), \tag{22}$$

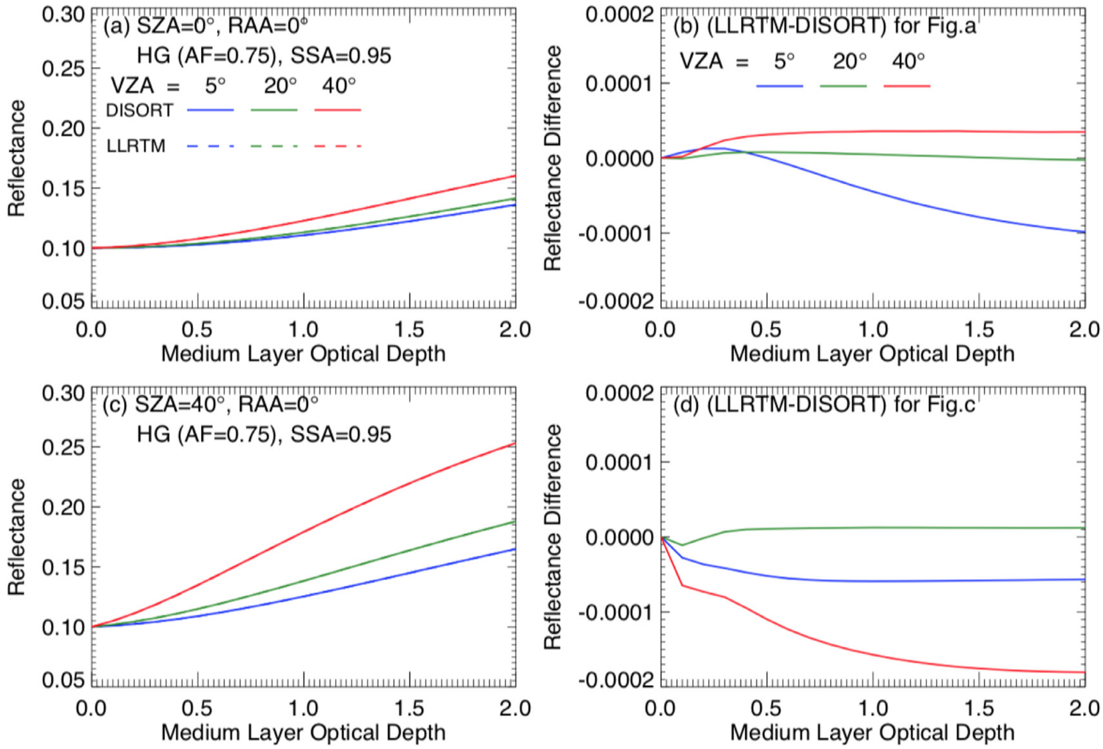

**Fig. A1.** Validation of the reflectance at the top of the atmosphere simulated by LLRTM based on the benchmarks from the DISORT model for a single scattering medium layer case. Figures (a) and (c) respectively represent the reflectance values simulated by LLRTM (dashed line) and DISORT (solid line) models with solar zenith angle (SZA)=0° (figure a) and 40° (figure b), view zenith angle (VZA)=5° (blue), 20° (green), and 40° (red), and relative azimuth angle (RAA)=0°. Figures (b) and (d) respectively represent the corresponding reflectance differences (LLRTM-DISORT) for Figures (a) and (c). The optical depth of the scattering medium layer ranges from 0.0 to 2.0 with a Henyey-Greenstein scattering phase function (asymmetry factor, AF = 0.75), a single scattering albedo (SSA) = 0.95, and a Lambert surface albedo = 0.10.

$$T_L(\mu,\phi;0,0) = \frac{\omega\Delta\tau_L}{4\mu\mu_0}P(\mu,\phi;0,0), \tag{23}$$

According to Eq. (17), the two independent source functions of $J_0$ (lunar) and $J_L$ (surface light source) under a single scattering approximation can be expressed as follows:

$$J_0(\tau;\mu,\phi) = \frac{\omega}{4\pi}F_0 P(\mu,\phi;-\mu_0,\phi_0)e^{-\tau/\mu_0}, \tag{24}$$

$$J_L(\tau_L;\mu,\phi) = \frac{\omega}{4\pi}F_1 P(-\mu,\phi;0,0)e^{-\tau_L}, \tag{25}$$

After that, the total $T$ and $R$ involving the two layers (subscripts 1, 2, and * respectively represent upper, lower, and the light beam from below) can be written as follows:

$$R_{12} = R_1 + T_1^* R_2 (1 - R_1^* R_2)^{-1} T_1, \tag{26}$$

$$T_{12} = T_2 (1 - R_1^* R_2)^{-1} T_1, \tag{27}$$

$$R_{12}^* = R_2^* + T_2 R_1^* (1 - R_2 R_1^*)^{-1} T_2^*, \tag{28}$$

$$T_{12}^* = T_1^* (1 - R_2 R_1^*)^{-1} T_2^*, \tag{29}$$

Note that, the incident beam flux of the surface light source comes from the bottom layer. Therefore, the adding-doubling equations use the reverse symbols in Eqs. (26–29) to calculate the RT process of the surface light source. Numerically, the AD method sets two adjacent optical layers $\tau_1 = \tau_2$ firstly. It starts with an optically thin layer $\Delta\tau = 10^{-6}$ and uses Eqs. (18–21) to compute the initial reflection and transmission functions at the first layer. Subsequently, Eqs. (26–29) are used to solve the reflection and transmission functions for the double optically thin layer of $\Delta\tau$, which will calculate iteratively in one single optical or atmospheric layer.

In the light of the definition in Eq. (16), after the calculation of $I^m$ at different quadrature azimuth angle from two various light sources, the total radiance intensity, $I$, at each layer, can be computed in the Fourier expansion form:

$$I(\tau;\mu,\phi) = \sum_{m=0}^{N} I_0^m(\tau;\mu) cosm\varphi + \sum_{m=0}^{N} I_L^m(\tau;\mu) cosm\varphi, \tag{30}$$

This radiance simulated by the LLRTM in this investigation is the observation value from the space-based low-light band with two different incident radiation sources. We use a classical Gauss-Legendre quadrature function to compute quadrature points for the zenith angle in this LLRTM.

To validate the performance of LLRTM, we use the discrete ordinates radiative transfer model (DISORT V2.0, http://lllab.phy.stevens.edu/disort) [41] as the benchmark to simulate the reflectance at the TOA scattered by a single medium layer. For the lack of the RT calculation capability for the surface light source, it only can validate the simulation reflectance or radiance under solar incident conditions based on the DISORT model. In this study, we use the Henyey-Greenstein (HG) phase function [42] to represent the light scattering properties of the single medium layer, which is written in a power form of asymmetry factor (AF), $g$, for the input of RTM

$$P_{HG,\,m} = (2m+1)\cdot g^m,\ (m = 0, 1, 2, \ldots N), \tag{31}$$

Same as Eq. (17), $m$ is the moment of Legendre polynomial. The sample code for calculating the HG scattering phase function is provided by the official test program of the DISORT V2.0 model.

Fig. A1 shows the reflectance results at the TOA simulated by LLRTM and DISORT models for a single scattering medium layer case under different optical depths (from 0 to 2) and observation geometries. The stream number of quadrature direction is 16 for both RTMs. Similar to Eq. (14), the definition of reflectance at the TOA is

$$\rho = \frac{\pi I}{\mu F_0}. \tag{32}$$

From this figure, we find a small difference (the maximum difference $< 0.0002$ or 0.1%) between LLRTM and DISORT under different conditions, which will slightly increase with the optical depth of the single medium layer. We set the single scattering albedo (SSA) $= 0.95$, and a Lambert surface albedo $= 0.10$ for all the validation cases. Therefore, the results indicate that the new LLRTM model can accurately simulate radiance or reflectance observed by the space-based low-light band under two different light sources.

## References

[1] Miller SD, Haddock SHD, Elvidge CD, Lee TF. Detection of a bioluminescent milky sea from space. Proc Natl Acad Sci 2005;102:14181–4.
[2] Li X, Xu H, Chen X, Li C. Potential of NPP-VIIRS nighttime light imagery for modeling the regional economy of China. Remote Sens (Basel) 2013;5:3057–81.
[3] Li X, Elvidge C, Zhou Y, Cao C, Warner T. Remote sensing of night-time light. Int J Remote Sens 2017;38:5855–9.
[4] Kieffer H, Stone T. The spectral irradiance of the moon. Astron J 2005;129:2887–901.
[5] Miller SD, Turner RE. A dynamic lunar spectral irradiance data set for NPOESS/VIIRS day/night band nighttime environmental applications. IEEE Trans Geosci Remote Sens 2009;47:2316–29.
[6] Elvidge CD, Baugh KE, Dietz JB, Bland T, Sutton PC, Kroehl HW. Radiance calibration of DMSP-OLS low-light imaging data of human settlements. Remote Sens Environ 1999;68:77–88.
[7] Miller SD, Mills SP, Elvidge CD, Lindsey DT, Lee TF, Hawkins JD. Suomi satellite brings to light a unique frontier of nighttime environmental sensing capabilities. Proc Natl Acad Sci 2012;109:15706–11.
[8] Elvidge CD, Cinzano P, Pettit DR, Arvesen J, Sutton P, Small C, et al. The Night-Sat mission concept. Int J Remote Sens 2007;28:2645–70.
[9] Cao C, Luccia FJD, Xiong X, Wolfe R, Weng F. Early on-orbit performance of the visible infrared imaging radiometer suite onboard the Suomi National Polar-orbiting Partnership (S-NPP) satellite. IEEE Trans Geosci Remote Sens 2014;52:1142–55.
[10] Lee S, Chiang K, Xiong X, Sun C, Anderson S. The S-NPP VIIRS day-night band on-orbit calibration/characterization and current state of SDR products. Remote Sens 2014;6:12427–46.
[11] Zhang G., Guo X., Li D., Jiang B. Evaluating the potential of LJ1-01 nighttime light data for modeling socio-economic parameters Sensors. 2019;19:1465.
[12] Hu X, Sun L, Liu J, Ding L, Wang X, Li Y, et al. Calibration for the solar reflective bands of medium resolution spectral imager onboard FY-3A. IEEE Trans Geosci Remote Sens 2012;50:4915–28.
[13] Min M., Cao G., Xu N., Bai Y., Jiang S., Hu X., et al. On-orbit spatial quality evaluation and image restoration of FengYun-3C/MERSI IEEE Trans Geosci Remote Sensing. 2016;54:6847–58.
[14] Zhang P, Yang L, Gu S, Hu X, Wu X, Wu R, et al. Meteorological requirements for the early-morning-orbit satellite. Adv Meteorol Sci Tech 2015;5:6–12.
[15] Peng Z, Qifeng L, Xiuqing H, Songyan G, Lei Y, Min M, et al. The latest progress of Chinese meteorological satellite program and core data processing technologies. Adv Atmos Sci 2019;36:1027–45.
[16] Kyba CCM, Kuester T, de Miguel AS, Baugh K, Jechow A, Hölker F, et al. Artificially lit surface of Earth at night increasing in radiance and extent. Sci Adv 2017;3:e1701528.
[17] Elvidge CD, Zhizhin M, Baugh K, Hsu FC, Ghosh T. Extending nighttime combustion source detection limits with short wavelength VIIRS data. Remote Sens (Basel) 2019;11:395.
[18] Miller SD, William C, Strak I, Yue J, Seaman CJ, Xu S, Elvidge CD, et al. The dark side of hurricane Matthew: unique perspectives from the VIIRS day/night band. Bull Am Meteorol Soc 2018;99:2561–74.
[19] Li X, Ma R, Zhang Q, Li D, Liu S, He T, et al. Anisotropic characteristic of artificial light at night – Systematic investigation with VIIRS DNB multi-temporal observations. Remote Sens Environ 2019;233:111357.
[20] Cao C, Bai Y, Wang W, Choi T. Radiometric inter-consistency of VIIRS DNB on Suomi NPP and NOAA-20 from observations of reflected lunar lights over deep convective clouds. Remote Sens (Basel) 2019;11:934.
[21] Wang X., Min M., Wang F., Guo J., Li B., Tang S. Intercomparisons of cloud mask product among Fengyun-4A, Himawari-8 and MODIS. IEEE Transactions on Geoscience and Remote Sensing. 2019.
[22] Miller SD, Straka W, Mills SP, Elvidge CD, Lee TF, Solbrig J, et al. Illuminating the capabilities of the Suomi national polar-orbiting partnership (NPP) visible infrared imaging radiometer suite (VIIRS) day/night band. Remote Sens (Basel) 2013;5:6717–66.
[23] Johnson RS, Zhang J, Hyer EJ, Miller SD, Reid JS. Preliminary investigations toward nighttime aerosol optical depth retrievals from the VIIRS day/night band. Atmos Meas Tech 2013;6:1245–55.
[24] Walther A, Heidinger AK, Miller S. The expected performance of cloud optical and microphysical properties derived from Suomi NPP VIIRS day/night band lunar reflectance. J Geophys Res 2013;118:13230–40.
[25] Min M, Deng J, Liu C, Lu N, Hu X, Chen L, et al. An investigation of the implications of lunar illumination spectral changes for day/night band based cloud property retrieval due to lunar phase transition. J Geophys Res - Atmosph 2017;122:9233–44.
[26] Min M, Zhang Z. On the influence of cloud fraction diurnal cycle and sub-grid cloud optical thickness variability on all-sky direct aerosol radiative forcing. J Quant Spectrosc Radiat Transfer 2014;142:25–36.
[27] Liou KN. An introduction to atmospheric radiation second edition. USA Elsevier Sci 2002.
[28] Buratti BJ, Hicks MD, Nettles J, Staid\ M, Pieters CM, Sunshine J, et al. A wavelength-dependent visible and infrared spectrophotometric function for the moon based on ROLO data. J Geophys Res - Atmosph 2011;116:E00G3.
[29] Kyba CCM, Ruhtz T, Fischer J, Hölker F, Kyba CCM, Ruhtz T, et al. J Geophys Res 2011;116:D24106.
[30] Kanda M, Kawai T, Nakagawa K. A simple theoretical radiation scheme for regular building arrays. Boundary Layer Meteorol 2005;114:71–90.
[31] Parichart C, Hagishima A, Tanimoto J. A computer system to support albedo calculation in urban areas. Build Environ 2004;39:1213–21.
[32] Wang J, Aegerter C, Xu X, Szykman JJ. Potential application of VIIRS day/night band for monitoring nighttime surface PM2.5 air quality from space. Atmos Environ 2016;124:55–63.
[33] Zhang Z, Yang P, Kattawar G, Huang HL, Greenwald T, Li J, et al. A fast infrared radiative transfer model based on the adding-doubling method for hyperspectral remote-sensing applications. J Quant Spectrosc Radiat Transf 2007;105:243–63.
[34] Clough SA, Shephard MW, Mlawer EJ, Delamere JS, Iacono MJ, Cady-Pereira K, et al. Atmospheric radiative transfer modeling: a summary of the AER codes. J Quant Spectrosc Radiat Transfer 2005;91:233–44.
[35] Srivastava SS, Vyas NK, Rai J, Kartikeyan B. On the different approaches of Rayleigh optical depth determination. Adv Space Res 2009;44:1058–66.
[36] Guo J, Li Y, Cohen J, Li J, Chen D, Xu H, et al. Shift in the temporal trend of boundary layer height trend in China using long-term (1979–2016) radiosonde data. Geophys Res Lett 2019;46:6080–9.
[37] Liu C, Yang P, Nasiri SL, Platnick S, Meyer KG, Wang C, et al. A fast visible infrared imaging radiometer suite simulator for cloudy atmospheres. J Geophys Res 2015;120:240–55.
[38] Liu Q, Boukabara S. Community radiative transfer model (CRTM) applications in supporting the suomi national polar-orbiting partnership (SNPP) mission validation and verification. Remote Sens Environ 2014;140:744–54.
[39] Wang C, Yang P, Platnick S, Heidinger AK, Baum BA, Greenwald T, et al. Retrieval of ice cloud properties from AIRS and MODIS observations based on a fast high-spectral-resolution radiative transfer model. J Appl Meteorol Climatol 2013;52:710–26.
[40] Evans KF, Stephens GL. A new polarized atmospheric radiative transfer model. J Quant Spectrosc Radiat Transf 1991;46:413–23.
[41] Stamnes K, Tsay SC, Wiscombe W, Jayaweera K. Numerically stable algorithm for discrete-ordinate-method. Appl Opt 1988;27:2502–9.
[42] Yang P, Bi L, Baum BA, Liou KN, Kattawar GW, Mishchenko MI, et al. Spectrally consistent scattering, absorption, and polarization properties of atmospheric ice crystals at wavelengths from 0.2 to 100 µm. J Atmospheric Sci 2013;70:330–47.